

Ageostrophic instabilities of fronts in a channel in a stratified rotating fluid

J. GULA†, R. PLOUGONVEN AND V. ZEITLIN

Laboratoire de Météorologie Dynamique, ENS, IPSL, Paris, France

(Received 4 February 2008 and in revised form 14 January 2009)

It is known that for finite Rossby numbers geostrophically balanced flows develop specific ageostrophic instabilities. We undertake a detailed study of the Rossby–Kelvin (RK) instability, previously studied by Sakai (*J. Fluid Mech.*, vol. 202, 1989, pp. 149–176) in a two-layer rotating shallow-water model. First, we benchmark our method by reproducing the linear stability results obtained by Sakai (1989) and extend them to more general configurations. Second, in order to determine the relevance of RK instability in more realistic flows, simulations of the evolution of a front in a continuously stratified fluid are carried out. They confirm the presence of RK instability with characteristics comparable to those found in the two-layer case. Finally, these simulations are used to study the nonlinear saturation of the RK modes. It is shown that saturation is achieved through the development of small-scale instabilities along the front which modify the mean flow so as to stabilize the RK mode. Remarkably, the developing instability leads to conversion of kinetic energy of the basic flow to potential energy, contrary to classical baroclinic instability.

1. Introduction

The study of instabilities of vertically sheared flows in rotating stratified fluids has provided understanding of important aspects of mid-latitude motions in the atmosphere and ocean, starting from the work of Eady (1949) on baroclinic instability. The latter has been identified as the major instability occurring for flows with small Rossby numbers. It is well described in balanced models such as the quasi-geostrophic model and can be interpreted in terms of the resonant interaction between two Rossby waves (Hoskins, McIntyre & Robertson 1985; Hayashi & Young 1987).

However, a vertically sheared flow in the stratified rotating fluid displays other instabilities as well. These are not captured by balanced approximations and hence are *ageostrophic* instabilities. They were first addressed for the uniform vertical shear in the stratified fluid by Stone (1966) who demonstrated appearance of symmetric instability. The Kelvin–Helmholtz instability also appears for non-uniform vertical shear profiles (Drazin & Reid 1981; Vanneste 1993). For intermediate values of the shear, both Stone (1970) and Tokioka (1970) identified other ageostrophic instabilities, at scales shorter than those of conventional baroclinic instability. These modes however have weaker growth rates, and it was hence argued that they would not be relevant (Stone 1970). Their structure involves inertial critical levels (Jones 1967) in the flow and the connection of balanced motions to inertia–gravity waves through that level (Nakamura 1988; Plougonven, Muraki & Snyder 2005). Corresponding growth rates

† Email address for correspondence: gula@lmd.ens.fr

are exponentially small for small Rossby numbers (Molemaker, McWilliams & Yavneh 2005), making them relevant only for significant vertical shears.

Baroclinic instability is traditionally explained with the help of the two-layer model (Phillips 1954). The stability of the ageostrophic version of the Phillips's model was studied by Sakai (1989), who showed the existence of unstable modes involving the resonance between a Rossby wave in one layer and a Kelvin wave in the other. Hence the instability was called Rossby–Kelvin (RK). In contrast to the results of Stone (1970), the growth rates of this instability proved to be comparable to or even larger than those of the baroclinic instability.

Sakai (1989) carried out the linear stability analysis for the two-layer fluid in a symmetric configuration which is known to be degenerate (Pedlosky 1987, §7.11), both layers having the same mean depth. Hence, several questions arise: (i) What are the manifestations of this instability in the more general case? (ii) Are the unstable modes and their growth rates specific to the two-layer configuration, or do they exist also in stratified fluid for sharp enough fronts? (iii) How do they nonlinearly saturate?

The fundamental motivation for the present study is that RK instability provides an example of coupling of balanced and unbalanced motions. Most of the dynamics of the atmosphere and oceans in mid-latitudes have been understood using balanced models (e.g. Pedlosky 1987). It has been thought that balanced motions could even decouple completely from unbalanced motions, leading to the notion of an exactly invariant *slow manifold* (Leith 1980; Lorenz 1980). It is now understood that *slow manifolds* are quasi-manifolds (Ford, McIntyre & Norton 2000); e.g. quasi-geostrophy defines one, and nonlinear balance defines a more accurate one. Yet the mechanisms by which balanced and unbalanced motions can couple and interact remain poorly understood. They have recently attracted renewed interest, from both theoretical (e.g. Plougonven & Zeitlin 2002; Vanneste & Yavneh 2004; Molemaker *et al.* 2005; Vanneste & Yavneh 2007) and experimental points of view (Afanasyev 2003; Williams, Haine & Read 2005), motivated by questions arising both for the atmosphere and for the ocean. In particular, in the laboratory experiments (Williams *et al.* 2005), the stability of fronts has been studied to identify the coupling of balanced and unbalanced motions. The interpretation of such experiments would benefit from a better understanding of the stability properties of intense fronts in a stratified rotating fluid.

Regarding the atmosphere, understanding of the coupling of balanced and unbalanced motions can contribute to a better identification of sources of gravity waves and their parameterizations. Indeed, a serious weakness of parameterizations of gravity waves in general circulation models of the atmosphere (Kim, Eckermann & Chun 2003; Fritts & Alexander 2003) is their lack of physical description of the sources of gravity waves. A major source in midlatitudes are tropospheric jets and fronts (Fritts & Nastrom 1992; Plougonven, Teitelbaum & Zeitlin 2003), which are essentially balanced. Another atmospheric application is understanding of the dynamics of secondary cyclogenesis in frontal systems. While the development and evolution of baroclinic waves on the synoptic scale is well understood in the atmosphere, the rapid growth of secondary cyclones at smaller scales is poorly understood and difficult to forecast (Parker 1998). Among the variety of mechanisms which contribute to small-scale cyclones, dynamic instabilities of a strong dry front are a possibility to investigate.

Regarding the ocean, an open issue is the mixing required to maintain the meridional overturning circulation. It is necessary that small-scale mixing in the interior of the

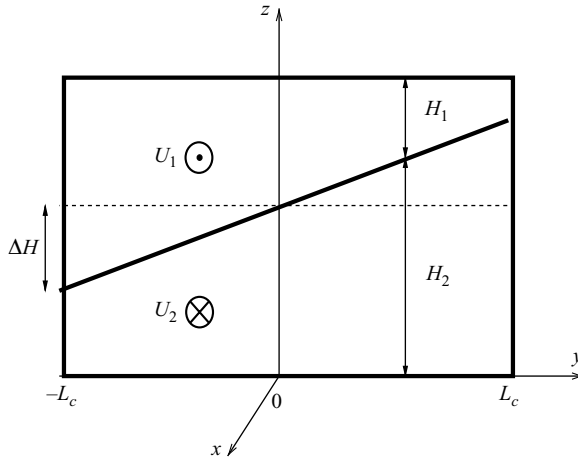


FIGURE 1. The basic balanced flow considered in the two-layer shallow-water model for $\delta = H_1(0)/H_2(0) = 0.7$ and $\lambda = \Delta H/H_2(0) = 0.5$.

oceans allows dense fluid to be raised towards the surface (Wunsch & Ferrari 2004). At present, it remains unclear how energy may cascade in the ocean interior from the balanced mesoscale circulations to small-scale unbalanced motions that lead to the vertical mixing (e.g. Molemaker *et al.* 2005). Ageostrophic instabilities may provide a path to energy dissipation at small scales and conversion of kinetic to potential energy.

The paper is organized as follows: in §2 we present the linear stability analysis of the balanced front in the two-layer fluid in various configurations; in §3 we study the stability of the sharp front in a continuously stratified fluid, using the atmospheric mesoscale model Weather Research and Forecasting (WRF); and in §4 the nonlinear evolution of the RK mode is discussed.

2. Linear stability analysis in the two-layer fluid

We first present the model and its linearized version and introduce the key parameters in §2.1. We then display the instabilities, their growth rates and the structure of the unstable modes in §2.2 and give a short summary of the results in §2.3

2.1. Overview of the model and the method

We consider the two-layer rotating shallow-water model on the f -plane with a vertical shear flow as shown in figure 1. The domain is a vertically bounded channel of width $2L_c$ and height $2H_0$. On the f -plane the momentum and continuity equations are

$$\left. \begin{aligned} D_j u_j - f v_j &= -\frac{1}{\rho_j} \partial_x \pi_j, \\ D_j v_j + f u_j &= -\frac{1}{\rho_j} \partial_y \pi_j, \\ D_j h_j + \nabla \cdot (h_j \mathbf{v}_j) &= 0, \end{aligned} \right\} \quad (2.1)$$

where the index $j = 1, 2$ denotes the upper and the lower layers, respectively; (x, y) and $\mathbf{v}_j = (u_j, v_j)$ are the along-channel and cross-channel coordinates and velocity components; $h_j = H_j(y) + (-1)^j \eta(x, y, t)$ are the depths of the layers with η the

interface displacement; π_j, ρ_j are the pressures and the densities of the layers; $D_j = \partial_t + u_j \partial_x + v_j \partial_y$ is the Lagrangian derivative; and f is the constant Coriolis parameter.

We linearize these equations about the steady geostrophically balanced state with the depth profiles $H_j(y)$ and corresponding velocities $U_j(y) = -(\rho_j f)^{-1} \partial_y \Pi_j$. The linearized equations, where u_j, v_j, π_j and η are the perturbations to the basic state fields, are

$$\left. \begin{aligned} \partial_t u_j + U_j \partial_x u_j + v_j \partial_y U_j - f v_j &= -\frac{1}{\rho_j} \partial_x \pi_j, \\ \partial_t v_j + U_j \partial_x v_j + f u_j &= -\frac{1}{\rho_j} \partial_y \pi_j, \\ \partial_t \eta + U_j \partial_x \eta &= (-1)^{j+1} (H_j \partial_x u_j + \partial_y (H_j v_j)). \end{aligned} \right\} \quad (2.2)$$

The dynamical boundary condition at the interface between the two layers is

$$\pi_2 - \pi_1 = (\rho_2 - \rho_1) g \eta, \quad (2.3)$$

where g is gravity acceleration.

In order to compare our results with those of the pioneering paper by Sakai (1989), the basic flow configuration and the non-dimensionalization are chosen to be the same. We will consider the basic state with $U_1 = -U_2 = U_0$ and correspondingly linear $H_j(y)$. This is an ageostrophic version of the Phillips's (1954) model, and both Rossby waves and inertia-gravity waves are present in this system.

We introduce the time scale $1/f$, the vertical scale $H_0 = H_2(0)$, the velocity scale U_0 and the pressure scale $\rho_j U_0 f R_d$. The Rossby deformation radius $R_d = ((1/2)g' H_0)^{1/2}/f$, with the reduced gravity $g' = 2\Delta\rho g/(\rho_1 + \rho_2)$, will be used as the horizontal scale. We will use only non-dimensional variables from now on without changing the notation. The following non-dimensional equations are obtained in the limit of the Boussinesq approximation ($(\rho_2 - \rho_1)/(\rho_2 + \rho_1) \rightarrow 0$):

$$\begin{aligned} \partial_t u_j + F U_j \partial_x u_j - v_j &= -\partial_x \pi_j, \\ \partial_t v_j + F U_j \partial_x v_j + u_j &= -\partial_y \pi_j, \end{aligned} \quad (2.4)$$

$$\begin{aligned} \partial_t \eta + F U_j \partial_x \eta &= (-1)^{j+1} (F (H_j \partial_x u_j + \partial_y (H_j v_j))), \\ \pi_2 - \pi_1 &= \frac{2}{F} \eta, \end{aligned} \quad (2.5)$$

where $F = U_0/(f R_d)$ is the Froude number. The boundary conditions are $v_j(\pm 1/(2\sqrt{Bu})) = 0$ at the lateral walls, and the Burger number $Bu = (R_d/(2L_c))^2$ controls the width of the channel. The height field is then written $H_j = H_j(0) + (-1)^j F y$.

Assuming a harmonic form of the solution in the x -direction,

$$(u_j(x, y), v_j(x, y), \pi_j(x, y)) = (\tilde{u}_j(y), \tilde{v}_j(y), \tilde{\pi}_j(y)) \exp [i(kx - \omega t)], \quad (2.6)$$

we obtain an eigenvalue problem of order six which can be solved by applying the spectral collocation method as described in Trefethen (2000) and Poulin & Flierl (2003). A complete basis of Chebyshev polynomials is used to obtain a discrete equivalent of the equations. This is achieved by evaluating (2.4) on a discrete set of N collocation points (typically $N = 50-100$). The eigenvalues and eigenvectors of the resulting operator are computed with MATLAB routine 'eig'. The occurrence of spurious eigenvalues is common in such discretization procedure. We therefore checked the persistence of the obtained eigenvalues by recomputing the spectrum with increasing N .

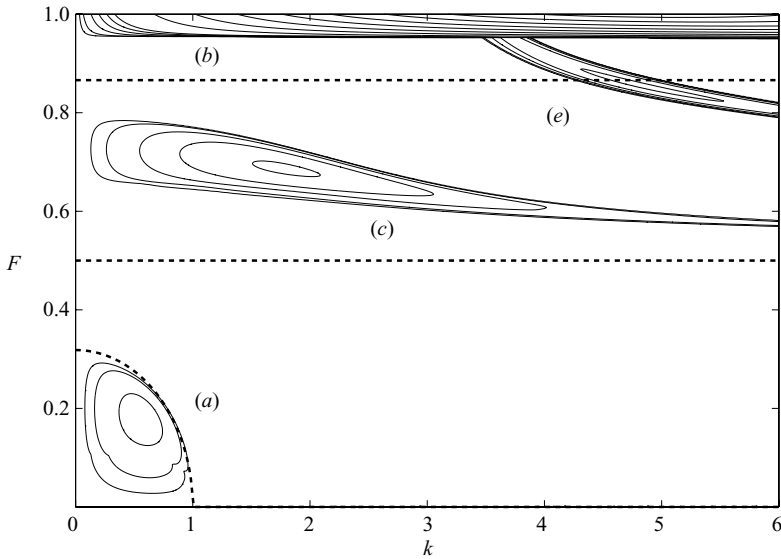


FIGURE 2. Growth rates of most unstable modes in (F, k) -space for $H_1(0) = H_2(0)$. Contours displayed are 0.01, 0.02 and further on at the interval 0.02. Dotted lines correspond to the limits of the instability zones (a) and (c) following from the frequency estimates and resonance conditions (see text).

2.2. Instabilities and growth rates

At this point we have three independent parameters which are the Froude number F , the Burger number Bu and the aspect ratio between the two layers δ . In order to explore parameter space using only one parameter for the flow, F , and the streamwise wavenumber k , Sakai (1989) restricted to a symmetric configuration, with $\delta = 1$, and chose to hold the relative elevation parameter $\lambda = F/(2\sqrt{Bu}) = 0.5$ constant, leading to $F = \sqrt{Bu}$. To facilitate the comparison with his results, we follow the same choice, but one should note the implication: as F varies, the width of the channel varies as λ/F . This unfortunately does not facilitate the comparison with laboratory experiments, such as those of Williams *et al.* (2005), where different non-dimensional parameters are chosen. Moreover, these experiments are carried out in a cylindrical annulus. To address these issues the corresponding linear stability analysis has been carried out in a companion paper (Gula, Zeitlin & Plougonven 2009).

The results of Sakai (1989) were reproduced, and the calculation in the symmetric configuration served as a benchmark of our method. The numerical results for the symmetric configuration are displayed in figure 2 and illustrate the different types of instabilities present in the symmetric configuration: (a) baroclinic instability for small F and k (the resonance between Rossby waves; see below); (b) Kelvin–Helmholtz instability for $F \approx 1$ (the resonance between Kelvin or inertia–gravity waves); (c), (e) RK in stability for $F \approx 0.7$ (the resonance between a Rossby wave and a Kelvin or inertia–gravity wave, respectively).

Following Ripa (1983) and Sakai (1989) the flow with velocity U_0 is unstable if there exists a pair of waves (intrinsic frequencies $\tilde{\omega}_1$ and $\tilde{\omega}_2$) which satisfy the following conditions: the waves propagate in the opposite directions with respect to the basic flow ($\tilde{\omega}_1\tilde{\omega}_2 < 0$, meaning that they have opposite energy anomalies), have almost the same Doppler-shifted (absolute) frequencies ($\tilde{\omega}_1 + kU_0 \sim \tilde{\omega}_2 - kU_0$) and

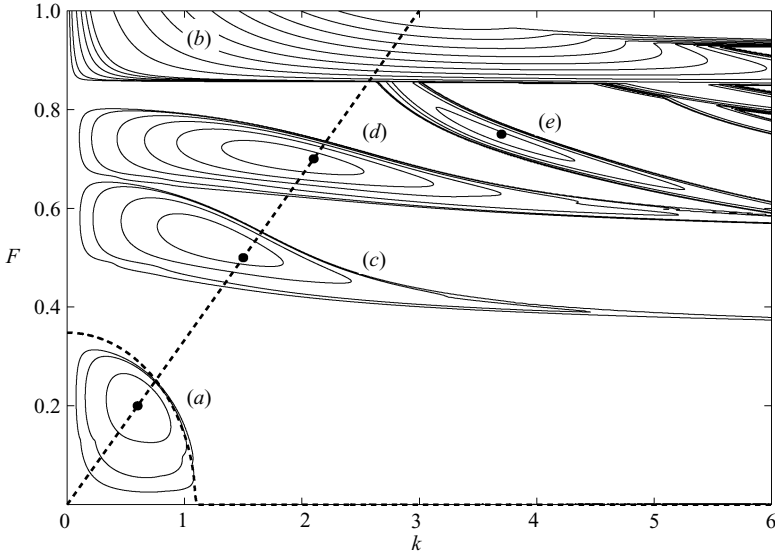


FIGURE 3. Growth rate of most unstable modes in (F, k) -space for $\delta = 0.7$. Contours displayed are 0.01, 0.02 and further interval 0.02: (a) is the baroclinic instability; (b) is the Kelvin–Helmholtz instability; and (c), (d), (e) are the RK instability.

can interact with each other. The interpretation of the unstable modes as resonances between the neutral waves provides the explanation for the regions of parameter space corresponding to different instabilities. Thus, the classical baroclinic instability is interpreted as the interaction between two Rossby waves propagating in each layer (see Hoskins *et al.* 1985). The condition of matching of Doppler-shifted frequencies for two Rossby waves gives the standard condition for the baroclinic instability to occur: $k^2 + l_n^2 < 1/\sqrt{\lambda}$ (Pedlosky 1987, § 7.11), where l_n is the meridional wave-number. Now, given the constraint linking the width of the domain and the Froude number, $F = \sqrt{Bu}$, l_n varies linearly with F , and more precisely $l_0 = \pi/(2L_c) = \pi F/(2\delta)$. Hence the region of parameter space corresponding to baroclinic instability in figures 2 and 3 lies within the quadratic curve:

$$k^2 + \left(\frac{\pi F}{2\lambda}\right)^2 < \frac{1}{\sqrt{\delta}}. \tag{2.7}$$

The RK instability can also be understood in terms of Kelvin and Rossby wave resonances. It is then possible to obtain stability conditions in the approximation of large k , using heuristic arguments for the resonance between the Kelvin and the Rossby wave. We estimate the absolute frequency for the Rossby wave as $\omega_R \simeq kF$ because the intrinsic frequency of Rossby waves is small for large k . The intrinsic frequency for the Kelvin wave in a layer of constant depth H can be written as $\tilde{\omega}_K = k\sqrt{g'H}$. Now, in our configuration the depth of each layer $H_j(y) = H_j(0) + Fy$ is a function of y . Using the extreme values of the depth of one layer gives bounds on the possible intrinsic frequencies of Kelvin waves in this layer: $\sqrt{2k}\sqrt{\delta \pm \lambda}$. Hence, it is most likely for a Rossby wave in one layer to interact with a Kelvin wave in the other layer, if we have

$$\sqrt{2k}\sqrt{H_j(0) - \lambda} < 2kF < \sqrt{2k}\sqrt{H_j(0) + \lambda},$$

with j the index of the layer containing the Kelvin wave. So if the Kelvin wave is in the upper layer and the Rossby wave in the lower layer we get

$$\sqrt{\frac{\delta - \lambda}{2}} < F < \sqrt{\frac{\delta + \lambda}{2}}, \tag{2.8}$$

and for the Kelvin wave in the lower layer and the Rossby wave in the upper layer we have

$$\sqrt{\frac{1 - \lambda}{2}} < F < \sqrt{\frac{1 + \lambda}{2}}. \tag{2.9}$$

In the symmetric configuration of figure 2 ($\lambda = 0.5$ and $\delta = 1$) this gives $0.5 < F < 0.85$ for both. This suggests that in this configuration and at least for large k there is a range of Froude numbers ($1/\pi^2 < F < 1/2$ in figure 2) in which no instability can occur. Although this condition has been obtained only for large k , it can be seen in figure 2, and it has been confirmed by numerical calculations that this stability area exists for all k . Increasing λ or changing the aspect ratio δ can modify this gap as can be seen in figure 3 for an asymmetric configuration ($\delta = 0.7$).

The configuration with the layers of the same mean depth is degenerate (Pedlosky 1987, §7.11). For example, the interaction between a Rossby wave in the lower layer and a Kelvin or inertia-gravity wave in the upper layer have the same characteristics (wavenumbers and growth rates) as the interaction between a Kelvin or inertia-gravity wave in the lower layer and a Rossby wave in the upper layer. Below we present an example of the results of the stability analysis for an asymmetric configuration, for which the depths of the two layers are not equal, $\delta = 0.7$ (which is the configuration sketched in figure 1). figure 3 shows the growth rates in the (F, k) -plane for different types of instabilities. At the lower left, for small F and k , one finds the baroclinic instability (*a*). For very strong shears, $F \approx 1$, Kelvin-Helmholtz instability occurs (*b*), with larger growth rates ($\omega_i \sim 1$). For intermediate values of the Rossby number, one finds two regions of instability ($F \approx 0.5$ for (*c*) and $F \approx 0.7$ for (*d*)) which correspond to RK instability. These instabilities exist due to the interaction of a Rossby wave in one layer and a Kelvin wave in the other. However, contrary to the symmetric case (cf. figure 2), two different RK instabilities occur, instead of a single one.

Figure 4 shows the phase velocities and the growth rates along the section $F = k/3$ following the dotted line in figure 3. Baroclinic instability (*a*) occurs for small k and Kelvin-Helmholtz instability (*b*) for k greater than 2.6. The two other peaks (*c*) and (*d*), for intermediate values of k are the two types of RK instability, with different growth rates. The dispersion diagram of figure 4 (upper panel) shows that the instability occurs once two dispersion curves intersect, according to the Doppler-shifted frequency matching described above. The dispersion curves shown in figure 4 differ from those of the symmetric case: whereas the Rossby wave phase speeds remain nearly symmetric relative to $c = 0$, the phase speeds for the Kelvin waves are displaced towards higher values. Hence, the intersection between the two modes moves towards higher k for positive phase speeds. We thus get two distinct instability areas. One corresponds to modes having a Kelvin wave in the upper layer and a Rossby wave in the lower layer. The structure of such a mode is shown in the left panel of the figure 5. The other corresponds to modes having a Kelvin wave in the lower layer and a Rossby wave in the upper layer (right panel of the figure 5). The characteristic velocities and pressure fields of the Rossby wave are easily recognizable with geostrophic wind turning around pressure extrema according to the geostrophic

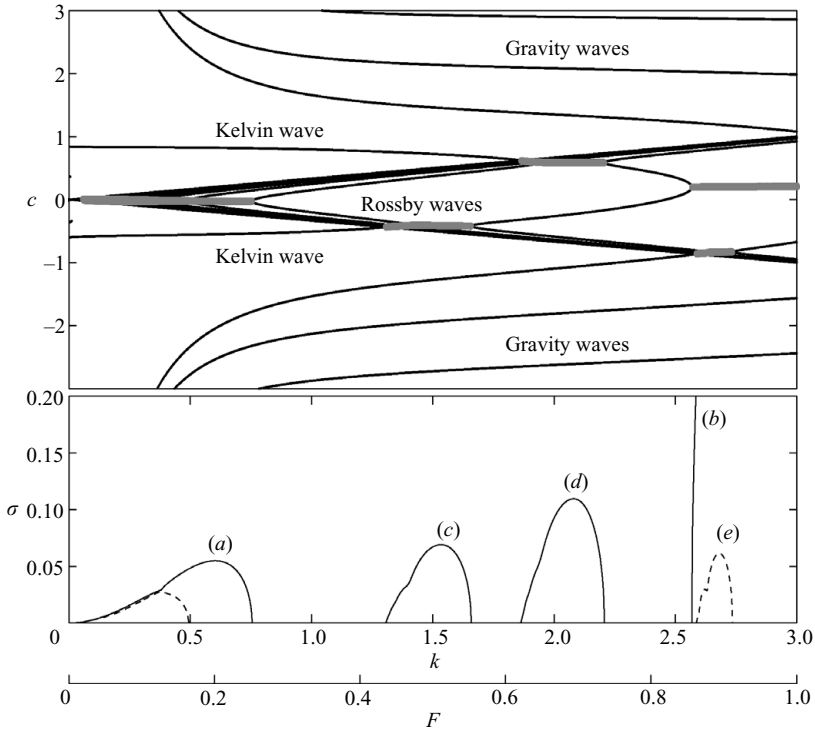


FIGURE 4. Dispersion diagram (upper panel) and growth rates (lower panel) of the eigenmodes along the section $F = k/3$ (dotted line in figure 3). Grey zones on the upper panel correspond to the instabilities: (a) the baroclinic instability; (b) the Kelvin–Helmholtz instability; and (c), (d), (e) the RK instability.

balance. The structure of the Kelvin waves with the wind parallel to the boundaries and pressure extrema near the lateral boundary is also clear and points out the ageostrophic character of this wave.

The instability area (e) in figure 3 is still a type of RK instability arising due to the resonance between a Rossby wave and an inertia–gravity wave (first Poincaré mode) as can be seen in figure 4. The Rossby wave propagating in the lower layer interacts with the first Poincaré mode in the upper layer as shown in figure 6. A simple criterion for this RK instability to occur as a result of resonance between a Rossby wave and a Poincaré wave can be found in Sutyrin (2007).

2.3. Summary of the linear instability analysis

We thus benchmarked our method by reproducing the linear stability results obtained by Sakai (1989) and extended them to asymmetric configurations in which two different families of unstable RK modes exist: one with the Kelvin wave in the top layer, the other with the Kelvin wave in the bottom layer. When the two layers have sufficiently different depths, the two regions separate, and hence a larger region of the parameter space yields instabilities (cf. figure 3). We have also shown that a zone of (relatively high) Froude numbers may exist, where neither baroclinic nor RK instability is present, and hence the flow is stable. The unstable RK modes are significant because of their large growth rates. This is in contrast with ageostrophic unstable modes found in flows with constant shear (Molemaker *et al.*

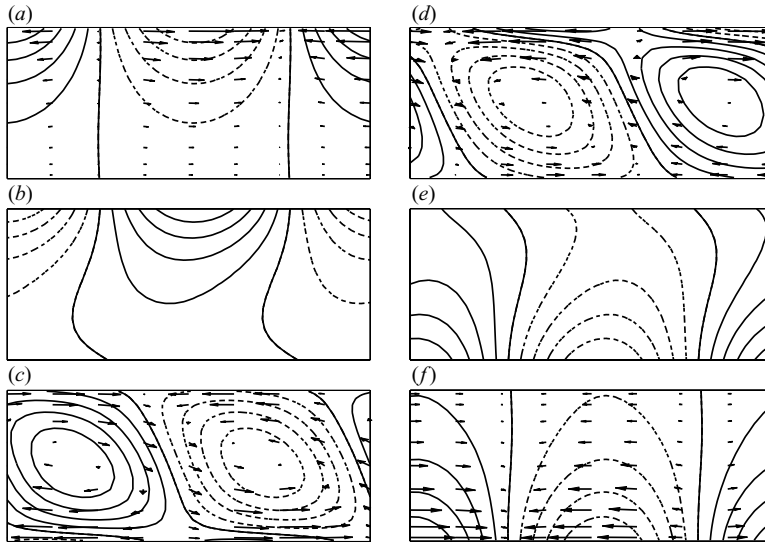


FIGURE 5. The structure of the RK mode in (x, y) at the maximum growth rate for $\delta = 0.7$: (a), (b) and (c) correspond to the second maximum of figure 4 for $F = 0.5$; (d), (e) and (f) correspond to the third maximum of figure 4 for $F = 0.7$; (a) and (d) are pressure and velocity fields of the upper layer; (c) and (f) are those of the lower layer. Interface height is shown in (b) and (e). The fields in (a) and (f) are typical of a Kelvin mode, and (c) and (d) are typical of a Rossby mode. The full lines correspond to positive and the dotted lines to negative values.

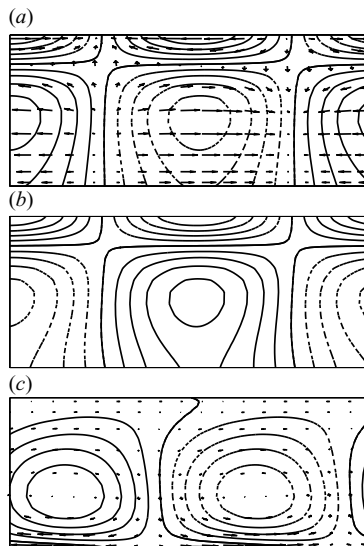


FIGURE 6. The structure of another ageostrophic mode in (x, y) due to the resonance between Rossby and inertia-gravity modes at the maximum growth rate for $F = 0.75$ and $k = 3.7$ on figure 4: (a) pressure and velocity fields in the upper layer and (c) lower layer; (b) interface height.

2005; Plougonven *et al.* 2005). However, as the RK modes have been exhibited only in the two-layer rotating shallow-water model, it is necessary to confirm that they also exist in a continuously stratified fluid.

3. RK instability in the continuously stratified fluid

We investigate below the instability of a front in a periodic channel by direct numerical simulations using the WRF model (Skamarock *et al.* 2005). This model has been developed to allow both operational and idealized simulations of fully compressible, non-hydrostatic atmospheric flows. The equations of motion are integrated in time using a third-order time-split Runge–Kutta scheme, and variables are discretized in space on a staggered Arakawa C-grid (Wicker & Skamarock 2002).

The model was chosen for its capacity to simulate flows of increasing complexity and realism, up to real-case studies. In previous investigations of the spontaneous generation of inertia–gravity waves from idealized baroclinic life cycles (Plougonven & Snyder 2005, 2007), the model has proved robust and able to provide a neat description of the weak emission of inertia–gravity waves by atmospheric jets and fronts.

First, we will present the model and the experimental set-up of the simulations (§3.1). Second, the most unstable modes for different sets of (F, k) parameters are described (§3.2). Finally the robustness of the RK modes with respect to changes of the basic flow and/or model parameters is investigated (§3.3). We will see that the front thickness and the background stratification has an effect on the growth rates even if the dynamics remain essentially the same.

3.1. The model and the experimental set-up

The domain is a channel of size (L_x, L_y, L_z) in the f -plane, periodic in x and bounded by lateral walls in y with a free-slip boundary condition. The free-slip boundary condition is imposed at the flat bottom as in the two-layer model of the previous section, and the top boundary is a free surface at constant pressure. Three main differences with the two-layer model are (i) the background stratification (in addition to the front), (ii) compressibility and its associated exponential decay of density in the vertical and (iii) the top boundary condition (free surface and not a rigid lid). These differences are not insignificant but should not affect the physical mechanisms providing the RK instability: if the unstable modes are robust, they will manifest themselves though with possible differences in the structure of velocity and pressure fields and in growth rates.

The basic state is defined by the strong localized gradient of potential temperature across the front:

$$\theta_{tot}(y, z) = \theta_0 + \Theta_z z + \frac{\theta_1}{2} \left(1 + \tanh \left(\frac{z - Z(y)}{D} \right) \right), \quad Z(y) = z_0 + S y, \quad (3.1)$$

where z_0 is the average height of the front; S is the slope; θ_1 is the potential temperature jump; D is the thickness of the frontal zone; and $\Theta_z = \text{constant}$ describes the basic stratification.

We obtain the balanced zonal jet configuration by assuming the thermal wind balance. As we consider a purely zonal flow, the thermal wind balance is an exact stationary solution of the full equations. Yet as described in Plougonven & Snyder (2007), the initial jet undergoes a minor adjustment when injected in WRF. Hence, to eliminate this adjustment the fields are averaged over two inertial periods, and the process is repeated twice, so that the adjustment associated with the background jet is negligible.

All variables in the WRF model are dimensional. Hence, it is necessary to choose a physical scale for the domain. We chose to work with typical tropospheric values of parameters: a domain height $L_z = 2 H_0 = 10$ km with a standard stratification

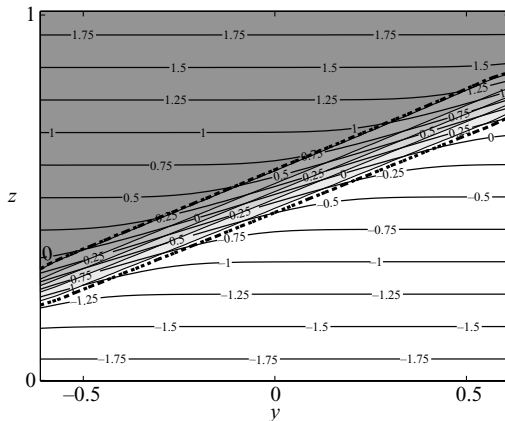


FIGURE 7. Initial distribution of potential temperature deviation θ (solid lines) and corresponding geostrophically balanced zonal wind (grey–white areas) for (z, y) . The contour intervals are 0.25 for the potential temperature and 0.5 for zonal wind speed. The dashed lines indicate zonal velocities $U = 0.25$ and $U = 1.9$, i.e. localization of the front zone.

$\Theta_z = \Theta_0/gN^2 = 2.9 \times 10^{-3} \text{ K m}^{-1}$ corresponding to a buoyancy frequency of $N^2 = 10^{-4} \text{ s}^{-2}$, a potential temperature $\theta_0 = 280 \text{ K}$ at the ground, a $\theta_1 = 10 \text{ K}$ potential temperature jump along the front and a $D = 500 \text{ m}$ thickness for the frontal zone. At this point the horizontal scale of the domain and the slope of the front (or the wind speed) have not been set. They are determined by the choice of the two non-dimensional numbers $F = U_0/(fR_d)$ and k , respectively the Froude number and the wavenumber.

The Rossby deformation radius is given by

$$R_d = \left(\frac{\frac{1}{2}g'H_0}{f^2} \right)^{1/2} = \left(\frac{g\theta_1 H_0}{2\theta_0 f^2} \right)^{1/2}, \quad (3.2)$$

and the Froude number is

$$F = \frac{U_0}{\sqrt{g'H_0/2}}. \quad (3.3)$$

We then describe the flow in the (F, k) -space analogous to the previous section, using the same relation between the channel width L_y and F as in Sakai (1989):

$$L_x = \frac{2\pi R_d}{k}, \quad L_y = 2\Delta H \frac{R_d}{F}. \quad (3.4)$$

From now on, the simulations are discussed only in terms of non-dimensional quantities, using the scalings θ_1 for the potential temperature deviation $\theta = \theta_{tot} - \theta_{mean}$, $2H_0$ for z , R_d for x and y and U_0 for all velocities. The initial state is shown in figure 7 for $F = 0.8$. Note that for simplicity we return here to a configuration with the two layers having equal mean depths, as in Sakai (1989). Yet because of compressibility and the top boundary condition, the two layers are no longer equivalent.

Our purpose is to determine whether the RK modes are present and robust for a balanced front in the continuously stratified fluid. Hence, simulations are initialized with a slightly perturbed front and carried out for various values of F and k in

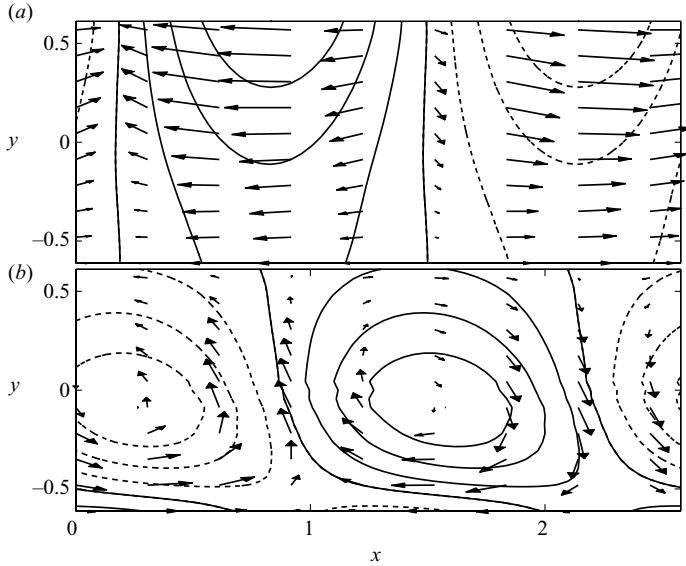


FIGURE 8. Vertically averaged pressure and velocity fields for the RK instability (a) above the front ($\theta > 0.5$) and (b) below the front ($\theta < -0.5$) for non-dimensional parameters $F = 0.8$ and $k = 2.4$. The full lines and the dotted lines indicate positive and negative values, respectively.

order to identify the unstable modes along the line $F = k/3$. A breeding procedure is applied in order to isolate the most unstable normal mode, if any, for each set of parameters used. The most unstable mode is computed by following the evolution of a small perturbation of the jet, then rescaling the perturbation to a smaller amplitude and starting the cycle again. The normal mode is then extracted, rescaled and superimposed upon the zonal jet. The simulations typically use 60 points for x and 40 for y with 80 levels in the vertical. We then vary the number of points and keep the grid length constant in order to sweep the (F, k) space.

3.2. Unstable modes

3.2.1. Baroclinic instability

For large enough domains ($F < 0.3$ and $k < 1$) the classical baroclinic instability occurs. Pressure and velocity fields correspond to Rossby waves in the lower and the upper part of the front. The spatial structure of the modes is very close to those found in the two-layer model (not shown). Growth rates are also very close to those of the two-layer model, as can be seen in figure 10 for $F < 0.3$. It is worth reminding that as is well known (see e.g. Holton 1992) the classical baroclinic instability leads to a conversion of available potential energy to kinetic energy.

3.2.2. The RK modes

The first key question is to determine whether the RK instability is also present in the continuously stratified case. The WRF simulations, as shown below, confirm the existence of these modes in the continuously stratified case, for values of F and k similar to those found in the two-layer model.

The RK modes of instability are indeed present in the stratified fluid, and their structure is comparable to that found in the two-layer model. Figure 8 shows the corresponding pressure and velocity fields vertically averaged below ($\theta < -0.5$) and

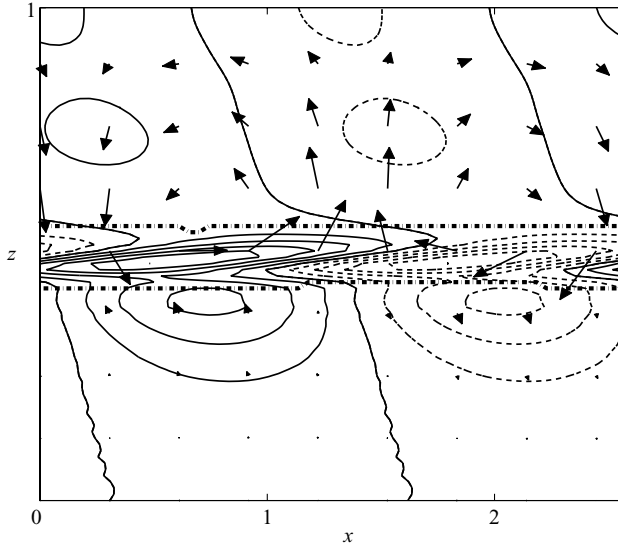


FIGURE 9. Velocity fields for the RK instability in the ($y=0$)-plane for non-dimensional parameters $F=0.8$ and $k=2.4$. Contours correspond to the meridional velocity with contour intervals 0.009. The dash-dotted lines indicates the interval in which the zonal velocity is between $U=0.25$ and $U=1.9$, i.e. localization of the front zone. Note the relatively strong vertical motion in the upper layer, indicating strong divergence of horizontal wind and hence unbalanced motions.

above ($\theta > 0.5$) the frontal zone. The structure of the geostrophically balanced Rossby wave can be identified clearly below the front, and the structure of the Kelvin wave (wind parallel to the boundaries, pressure extrema at the lateral boundaries) can be identified above the front. In the horizontal plane, the signature of this mode is very close to its counterpart in the two-layer model.

Figure 9 shows the velocity fields in the (x, z)-plane at $y=0$. Two features should be emphasized: Firstly, the modes clearly couple motions of very different nature, i.e. balanced motions in the lower layer that are essentially non-divergent and unbalanced motions in the upper layer that have significant signatures in the vertical velocity and hence in the divergence of the horizontal wind. Secondly, the signature of the mode is concentrated near the front. In other words, although the horizontal structure of the mode when averaged over each layer (figure 8) is very close to that found in the two-layer model, the motions are not at all homogeneous in the vertical in each layer.

3.2.3. Growth rates

The growth rates are evaluated from the growth of kinetic energy of the perturbation over the whole domain. Figure 10 shows the corresponding non-dimensional growth rates comparable to those found for the two-layer model (cf. Sakai 1989, figure 7). The maximum growth rate of the instability attained for $k=2.5$ is about $\sigma=0.09$ scaled by f^{-1} , so $\sigma^{-1}=1.25$ days.

3.3. Sensitivity of the results

Below we describe how the RK instability is influenced by the choice of the thickness of the frontal zone, by the value for the background stratification and, finally, by the resolution.

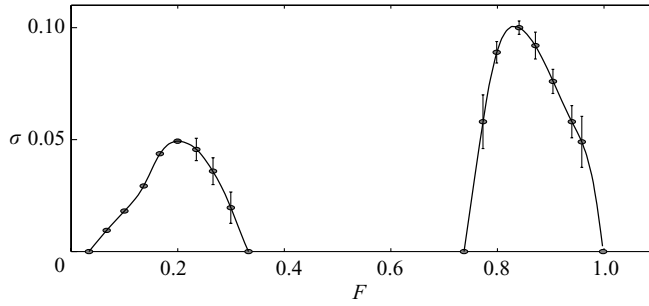


FIGURE 10. Growth rates of the instabilities of the front in the continuously stratified fluid. The peak at low k corresponds to the standard baroclinic instability. The peak for larger k corresponds to the RK instability.

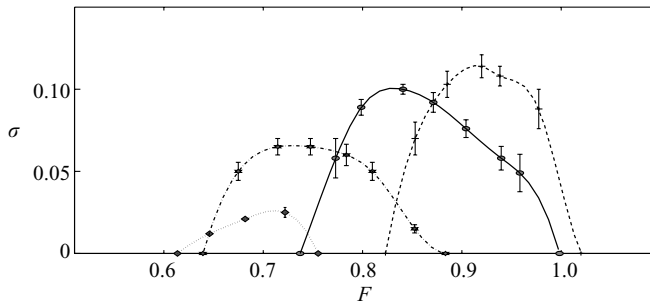


FIGURE 11. Growth rates for the RK mode of figure 8 for different basic stratifications. The dotted line corresponds to $\Theta_z = 0$, the dash-dotted line to $\Theta_z = 1.45$, the solid line to $\Theta_z = 2.9$ and the dashed line to $\Theta_z = 5.8$.

3.3.1. Stratification

To see whether the RK modes and their growth rates are sensitive to the background stratification, simulations have been carried out for cases with no stratification, with half stratification and double stratification, relative to the reference stratification described above

Changing the basic stratification Θ_z in the initial potential temperature distribution (cf. (3.1)) from $\Theta_z = 0$ to $\Theta_z = 1.45$, $\Theta_z = 2.9$ and $\Theta_z = 5.8$ modifies the growth rates, as can be seen from the figure 11. The maximum growth rate becomes smaller as the stratification parameter becomes lower, and the RK instability shifts to a smaller k . With a stratification weaker than in the reference simulation we were also able to find a RK mode consisting of a Kelvin wave below the front and a Rossby wave above for greater k . Corresponding pressure and velocity fields averaged above and below the front are shown in figure 12. However, these modes are less robust and seem to disappear as the background stratification increases.

3.3.2. Front thickness

In going from the two-layer fluid to a continuously stratified fluid with two well-defined layers, the thickness of the transition between the two layers, i.e. of the front, is a free parameter. It is essential to verify the sensitivity of the RK modes to the sharpness of the front.

For the reference simulations described in §3.2, a value of $D = 0.05$ was chosen for the front thickness (3.1). Simulations were also run for values of D ranging from

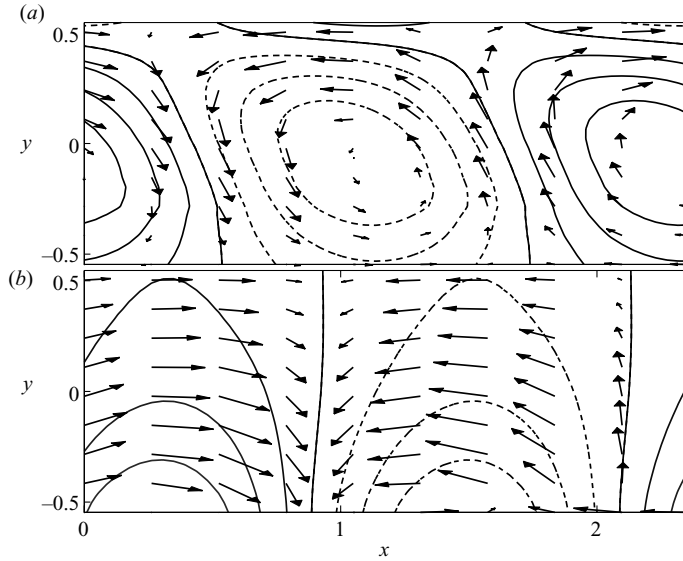


FIGURE 12. Pressure and velocity fields for a RK instability vertically averaged (a) above the front ($\theta > 0.5$) and (b) below the front ($\theta < -0.5$) for a simulation with half stratification and non-dimensional parameters $F = 0.87$ and $k = 2.6$.

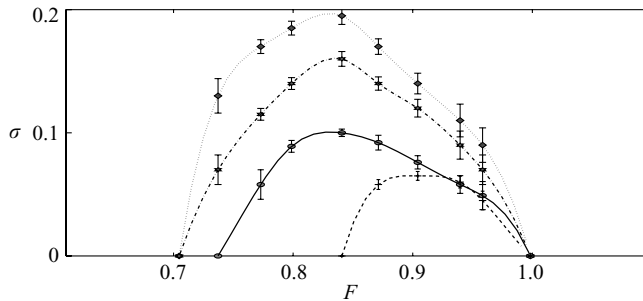


FIGURE 13. Growth rates for the RK mode of figure 8 for different thicknesses of the frontal zone. The values of D are 0.03 (dotted line), 0.04 (dash-dotted line), 0.05 (solid line) and 0.06 (dashed line).

0.03 to 0.06, in the interval of F and k likely to reveal the RK instability. The simulations show that the RK modes are indeed quite sensitive to the thickness of the front, as can be seen from the growth rates plotted in figure 13. The growth rates increase significantly (up to a factor 2) as the front becomes sharper and decrease for more diffuse fronts. Moreover, the range of wavenumbers k yielding instability is reduced for more diffuse fronts. Simulations were also carried out for front thicknesses $D \geq 0.16$ but did not exhibit robustly the presence of the RK modes or the growth of any other unstable ageostrophic mode.

3.3.3. Resolution

As in any numerical study, the sensitivity of the results to resolution needs to be checked. By definition, the initial front has regions of sharp vertical and horizontal gradients (figure 7). Sharp gradients concentrated in the vicinity of the front are also

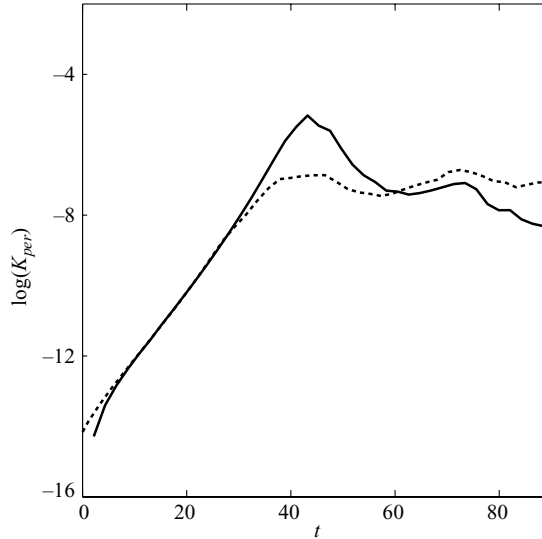


FIGURE 14. Logarithm of the kinetic energy K_{per} of the perturbation for the RK instability (normalized by initial total kinetic energy) for mode 1 in x , as a function of time. The dashed line shows the energy evolution for the simulation with double resolution as described in §3.3.3.

found in the structure of the unstable modes (figure 9). Hence it is essential to verify how sensitive the above results are to the resolution.

The simulations described above typically had a resolution of 60 points in x , 30 points in y and 80 points in z . Simulations have been run with a resolution doubled relative to the reference run, and it was found that the linear stability results were unchanged: the RK modes grew having the same structure and the same growth rate. As an example, figure 14 shows the variation of kinetic energy with time for two simulations with $F = 0.8$ and $k = 2.4$, the first with a domain having 60 points in x , 30 points in y and 80 points in z , the second with twice as many points in all directions. During the linear stage, the two curves overlap, indicating that the growth rate is not sensitive to the resolution. The structure of the RK mode as described in figures 8 and 9 is also the same in both simulations. Hence, the results described above are robust and not sensitive to the resolution.

4. Nonlinear evolution of the RK instability

Previous studies of ageostrophic unstable modes of fronts have addressed the linear stability problem (Sakai 1989; Iga 1993). To understand the importance that such ageostrophic modes may have in practice, it is necessary to investigate their nonlinear development and in particular to answer two questions: Do they grow to significant amplitudes? How do they saturate? The simulations carried out with WRF have the advantage of providing the answers to both questions. Below we will focus on two simulations with parameters $F = 0.8$ and $k = 2.4$: the reference run (as described in the previous section) and the corresponding run with double resolution.

First, the overall signature of the instability in the energy budget is discussed (§4.1). Second, the features of the flow that appear at the saturation of the RK modes are described (§4.2). These are found to be small-scale structures localized near one of the boundaries. Finally, the nonlinear effects due to the small-scale processes and

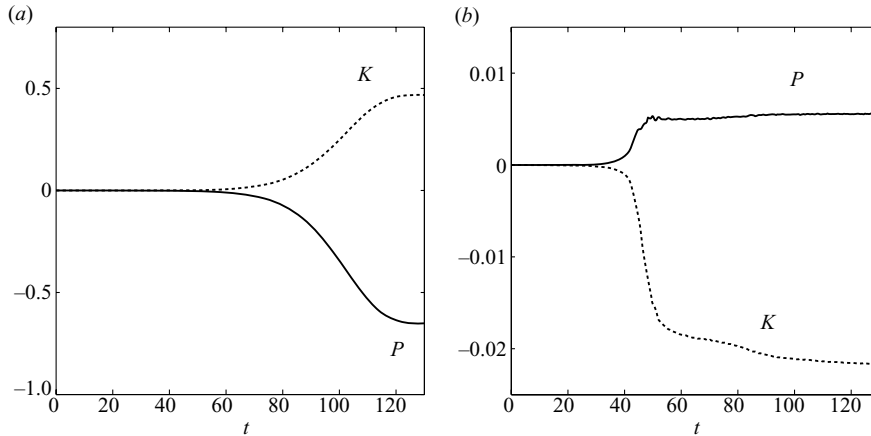


FIGURE 15. Deviations of the total potential (solid) and kinetic energy (dashed) of the flow during the growth stage of (a) the baroclinic instability ($F = 0.2$, $k = 0.6$) and (b) the RK instability ($F = 0.8$, $k = 2.4$). Both energies are normalized by the initial total kinetic energy of the flow.

their influence on the background mean flow is displayed (section 4.3), allowing for interpretation of the saturation of the RK modes.

4.1. Saturation and energetics

We first discuss the growth of the RK instability looking at the kinetic energy of the perturbation and then investigate the signature of the RK instability on the energetics of the total flow. We define the kinetic energy of the perturbation as

$$K_{per} = \iiint \frac{1}{2} \rho (u'^2 + v'^2 + w'^2) dx dy dz, \quad (4.1)$$

where $u' = u - \langle u \rangle = u - (1/L_x) \int_0^{L_x} u dx$. Energies are calculated dimensionally and then scaled by the kinetic energy of the basic flow. In both runs the instability grows exponentially up to $t \sim 40$ and then saturates, as can be seen in figure 14. It can be verified that the zonal wavenumber 1 mode (figure 8) is by far the most energetic.

To discuss the energy budget of the instability we define

$$K = \iiint \frac{1}{2} \rho (u^2 + v^2 + w^2) dx dy dz, \quad P = \iiint \rho (gz + c_v T) dx dy dz, \quad (4.2)$$

where K is the total kinetic energy of the flow and P is the total potential energy obtained as the sum of the gravitational potential energy and the internal energy (see Holton 1992, §8.3). The total energy conservation is then written

$$\frac{d}{dt} [K + P] = 0. \quad (4.3)$$

In practice, we do not expect that the total energy will be exactly conserved in the simulations because of numerical dissipation. The deviations of potential and kinetic energies from their initial values are shown in figures 15(b) for RK instability and, for reference, 15(a) for baroclinic instability. While plotting the energy we used the reference simulation (figures 8 and 9), but the energetics of the double resolution simulation described in §3.3.3 show a very similar behaviour.

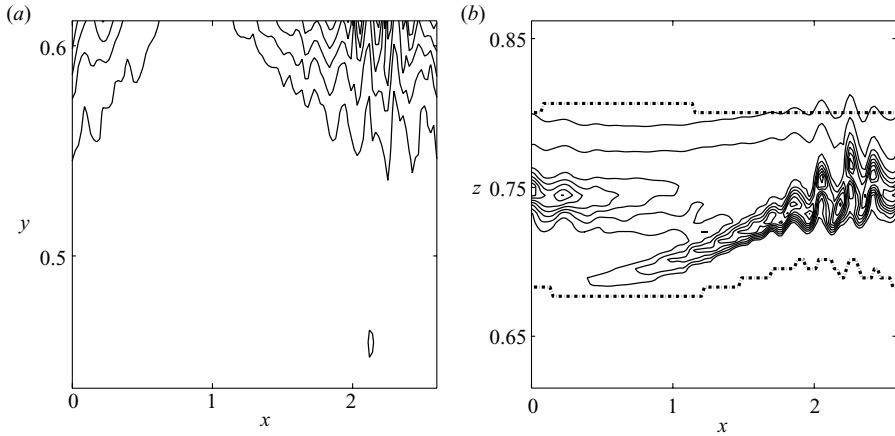


FIGURE 16. (a) Horizontal plot of the maximum along each vertical line of the y -component of relative vorticity; (b) y -component of relative vorticity in the (x, z) -plane close to the northern boundary ($y = 0.6$) after the RK saturation ($t = 40$ in figure 14). The dash-dotted lines indicate the localization of the front as in figure 7.

In sharp contrast with the classical baroclinic instability (see Holton 1992), the RK modes are found to convert kinetic energy of the basic flow into potential energy. However, one must also note that the variations of energy due to the classical baroclinic instability are stronger by a factor of 25. Hence RK instability has an effect on the basic flow which is the opposite of that of baroclinic instability (conversion of kinetic to potential energy), but the energies exchanged are much smaller.

Finally, one can note in figure 15 that the sum of potential and kinetic energies is not exactly conserved for both simulations. For the case of baroclinic instability the energy loss because of numerical dissipation represents about 15 % of the exchanged energies. For RK instability, it represents 60 %. The difference is likely due to the effective generation of the small-scale motions involved in the saturation of the instability, as discussed below.

4.2. Small-scale instabilities

Inspection of the simulations shows that the saturation of RK instability involves intense small-scale motions, developing near the lateral boundary to which the Kelvin wave is attached. The highest resolution simulation as described in § 3.3.3 is used to resolve this small-scale dynamics as well as possible. Figure 16 shows the relative vorticity of the flow at the time when the amplitude of the perturbation is maximal ($t = 40$). In addition to the zonal wavenumber 1 signature of the RK mode, intense small-scale features are found near the northern boundary where the Kelvin wave propagates. The small-scale features appear to be the result of the Kelvin–Helmholtz-type shear instabilities. They are particularly intense in the frontal region and generate quite intense vertical velocities above and below (not shown).

It is not surprising that the development of the RK modes leads to small-scale shear instabilities in the region of the front. Because the instability robustly appears only for sharp enough fronts (cf. § 3.3.2), the front in the basic state is already associated with low Richardson numbers $Ri = N^2 / (du/dz)^2 < 0.5$. Any motion will *a priori* modulate the front and the associated Ri . During the growth stage of the instability this will almost unavoidably lead to regions with $Ri < 0.25$, and shear instability is likely to occur. It was verified in the simulation that the small-scale instabilities

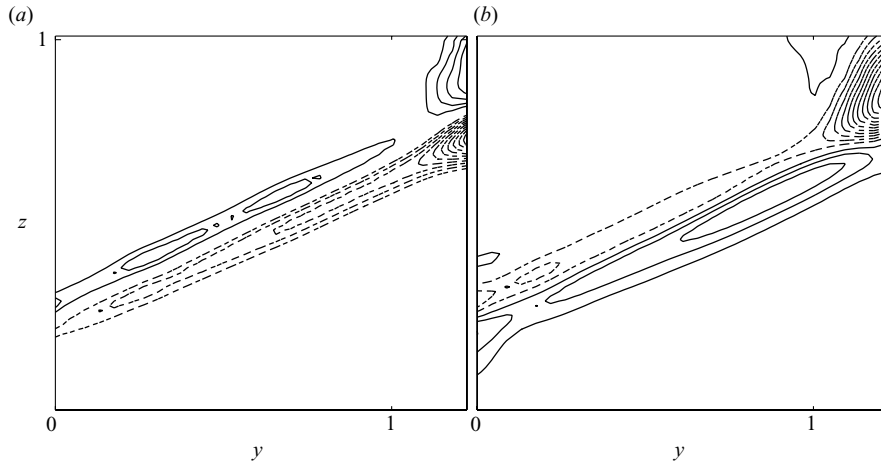


FIGURE 17. (a) Potential temperature deviation and (b) zonal mean flow deviation from the initial state (figure 7) after the RK mode saturation (cf. figure 14). The contour intervals are (a) 0.25 K m^{-1} and (b) 2 m s^{-1} .

develop in regions in which Ri is minimal (less than 0.1), due to the compression of the front associated with the RK mode. (Indications of this may be seen in figure 16*b*.)

Now, the small-scale motions are only barely resolved: the horizontal resolution of the simulation is about $dx = 0.022$, while the small-scale motions have a spatial wavelength $\lambda_x = 0.125$, which means about six grid points per wavelength. In the reference run, similarly, their wavelength is about $\lambda_x = 0.25$, again corresponding to about six grid points. To check the importance of the small-scale aspects of the flow, we have investigated the sensitivity of our results to diffusion. We used the standard second-order scheme for diffusion, in the horizontal directions alone or in the horizontal and vertical directions. However, a crucial point to note is that the front in the basic state is itself a small-scale feature and therefore is affected by the diffusion. For too large values of the diffusivity, typically values of the related Reynolds number less than $Re \sim 2000$ (calculated based on the grid size), the diffusion of the front precedes the development of RK instability. Comparatively, the development of the classical baroclinic instability is much more robust and persists for Reynolds numbers about $Re \sim 100$ or less in our simulations. For larger values of the Reynolds number, the diffusion was not found to alter significantly the dynamics described above. Hence it appears that the dissipation introduced in the last simulations did not have any significant effects on the small-scale dynamics involved in the saturation of the RK instability.

4.3. Mean flow response

The saturation of the RK mode can be understood by describing the effect of the small-scale motions on the mean zonal flow. These motions develop where the RK mode most strongly modulates the front, i.e. on the lateral boundary to which the Kelvin wave is attached. The modifications of the zonally averaged flow due to the small-scale instabilities are shown in figure 17. The main modifications are the broadening of the frontal zone and a deceleration of the zonal flow in the

upper layer and near the northern boundary, i.e. where the Kelvin wave was most intense.

As the velocities in the upper layer are reduced, conditions for the propagation of Kelvin waves are significantly changed. It appears that this mechanism is sufficient to break the conditions for the existence of the unstable mode, which essentially disappears after it has saturated (cf. figure 14). Indeed as the zonal velocity of the mean flow decreases close to the northern boundary of the upper layer, the Kelvin wave has a greater phase speed. (It is propagating against the flow.) The Rossby wave in the lower layer will keep the same phase speed, as the mean flow speed does not change in the lower layer. Hence it will become more difficult to couple the two waves by making the Doppler-shifted phase velocities coincide. The corresponding unstable mode will have a weaker growth rate, if any.

In order to verify this point, the linear stability of the two-layer model was revisited for a flow in which the velocity of the upper layer decreases near the appropriate lateral boundary. It was found that the existence of the RK modes was indeed very sensitive to the deceleration of the flow there and that the mode disappears if the deceleration was sufficient, which supports our interpretation.

Simulations which exhibited an RK mode with the Kelvin wave in the lower layer near the southern boundary provided further support for this interpretation. In these simulations the small-scale instabilities lead to a broadening of the frontal zone and a deceleration of the flow in the lower layer near the southern boundary, again changing the propagation conditions for the Kelvin wave in a way such that the RK mode disappears.

5. Summary

The linear stability of a front in a rotating, stratified fluid has been investigated with a focus on the ageostrophic modes of instability. These are by construction absent in the balanced models, such as the quasi-geostrophic approximation (e.g. Pedlosky 1987), and hence constitute an example of coupling of balanced and unbalanced motions. Key questions regarding these modes are to determine their structure and growth rates and to understand how they nonlinearly saturate.

Our starting point was the investigation by Sakai (1989) of the linear stability of a front in a rotating two-layer fluid, confined between vertical walls and horizontal surfaces. We have used a collocation method (Poulin & Flierl 2003) to re-examine Sakai's configuration and extend the results to more general configurations. Configurations with layers of different depths exhibited two different families of RK modes: one with the Kelvin wave in the top layer, the other with the Kelvin wave in the bottom layer. When the two layers have sufficiently different depths, the two regions separate, and hence a larger region of parameter space yields instabilities (cf. figure 3).

The unstable modes appear significant because of their relatively large growth rates. This is in contrast with ageostrophic unstable modes found for flows having constant shear (Molemaker *et al.* 2005; Plougonven *et al.* 2005). However, as RK modes have been previously exhibited only in the two-layer rotating shallow-water model, it was necessary to confirm that these modes also exist in a continuously stratified fluid and to investigate their sensitivity to the sharpness of the front. To answer these questions, numerical simulations of the evolution of a sharp front in a stratified atmosphere were carried out with an idealized configuration of the WRF model (Skamarock *et al.* 2005). The considered background state was comparable to the two-layer

model (sharp front confined by two lateral walls) but was more realistic in several aspects (background mean stratification, upper boundary condition, compressibility). Nevertheless, the RK modes were found to be present, demonstrating the robustness of the ageostrophic modes identified using the two-layer model. For sufficiently sharp fronts, the structure and growth rates of the modes were found to be comparable to the ones found in the two-layer model. However, sensitivity experiments showed that the growth rates of the modes were quite sensitive to the thickness of the front: they developed only for fronts having non-dimensional thicknesses smaller than 0.15.

Once the presence of the RK modes in the continuously stratified fluid was established, their nonlinear behaviour was investigated with the following important conclusions: (i) The modes grow to finite amplitude but retain energy levels that are small relative to the energy levels reached by the standard baroclinic instability. (ii) their saturation involves small-scale instabilities, presumably Kelvin–Helmholtz-type shear instabilities, in the region in which the growing RK mode increases the shear of the front sufficiently. These instabilities develop near the lateral boundary where the Kelvin wave propagates. Their effect on the zonal flow is concentrated within the frontal zone in the vertical and near the boundary where the Kelvin wave was present in the horizontal. The deceleration of the flow there changes the conditions for wave propagation and hence breaks the conditions for the existence of the unstable mode, which essentially disappears. (iii) Although the details of the saturation may not be entirely reliable due to resolution limitations, the effect of the unstable modes on the energy budget is clear: contrary to the classical baroclinic instability, kinetic energy is converted to potential energy. (In the simulations presented, about 2% of the kinetic energy is lost.) The fact that RK instability leads to a conversion of kinetic energy to potential energy could be of particular interest in the oceanic context (cf. Wunsch & Ferrari 2004). However, because the unstable modes are found to saturate at small amplitude and because they are described here in a specific configuration with lateral walls, its significance in the open water is to be further investigated.

Further study of the stability of fronts is under way for related configurations – in an axisymmetric annulus, with applications to laboratory experiments in mind, and for a front that intersects either of the horizontal surfaces, with both oceanic and atmospheric situations in mind.

The authors thank Jacques Vanneste for fruitful discussions and helpful suggestions on this problem. The calculations were carried out at IDRIS, France. This work was supported by ANR project FLOWINg (BLAN06-3 137005) and Alliance project 15102ZJ.

REFERENCES

- AFANASYEV, Y. 2003 Spontaneous emission of gravity waves by interacting vortex dipoles in a stratified fluid: laboratory experiments. *Geophys. Astrophys. Fluid Dyn.* **97** (2), 79–95.
- DRAZIN, P. G. & REID, W. H. 1981 *Hydrodynamic Stability*. Cambridge University Press.
- EADY, E. T. 1949 Long waves and cyclone waves. *Tellus* **1**, 33–52.
- FORD, R., MCINTYRE, M. E. & NORTON, W. A. 2000 Balance and the slow quasimanifold: some explicit results. *J. Atmos. Sci.* **57**, 1236–1254.
- FRITTS, D. C. & ALEXANDER, M. J. 2003 Gravity wave dynamics and effects in the middle atmosphere. *Rev. Geophys.* **41** (1), 1003.

- FRITTS, D. C. & NASTROM, G. D. 1992 Sources of mesoscale variability of gravity waves. Part 2. Frontal, convective, and jet stream excitation. *J. Atmos. Sci.* **49** (2), 111–127.
- GULA, J., ZEITLIN, V. & PLOUGONVEN, R. 2009 Instabilities of two-layer shallow-water flows with vertical shear in the rotating annulus. Submitted.
- HAYASHI, Y.-Y. & YOUNG, W. R. 1987 Stable and unstable shear modes of rotating parallel flows in shallow water. *J. Fluid Mech.* **184**, 477–504.
- HOLTON, J. R. 1992 *An Introduction to Dynamic Meteorology*, 3rd edn. Academic.
- HOSKINS, B. J., MCINTYRE, M. E. & ROBERTSON, A. W. 1985 On the use and significance of isentropic potential vorticity maps. *Q. J. R. Meteorol. Soc.* **111** (470), 877–946.
- IGA, K. 1993 Reconsideration of Orlanski's instability theory of frontal waves. *J. Fluid Mech.* **255**, 213–236.
- JONES, W. L. 1967 Propagation of internal gravity waves in fluids with shear flow and rotation. *J. Fluid Mech.* **30**, 439–448.
- KIM, Y.-J., ECKERMANN, S. D. & CHUN, H.-Y. 2003 An overview of the past, present and future of gravity-wave drag parametrization for numerical climate and weather prediction models. *Atmos.-Ocean* **41**, 65–98.
- LEITH, C. E. 1980 Nonlinear normal mode initialization and quasi-geostrophic theory. *J. Atmos. Sci.* **37**, 958–968.
- LORENZ, E. N. 1980 Attractor sets and quasi-geostrophic equilibrium. *J. Atmos. Sci.* **37**, 1685–1699.
- MOLEMAKER, M. J., MCWILLIAMS, J. C. & YAVNEH, I. 2005 Baroclinic instability and loss of balance. *J. Phys. Oceanogr.* **35**, 1505–1517.
- NAKAMURA, N. 1988 Scale selection of baroclinic instability: effects of stratification and nongeostrophy. *J. Atmos. Sci.* **45** (21), 3253–3267.
- PARKER, D. J. 1998 Secondary frontal waves in the North Atlantic region: a dynamical perspective of current ideas. *Q. J. R. Meteorol. Soc.* **124**, 829–856.
- PEDLOSKY, JOSEPH 1987 *Geophysical Fluid Dynamics*, 2nd edn. Springer.
- PHILLIPS, N. A. 1954 Energy transformations and meridional circulations associated with simple baroclinic waves in a two-level, quasi-geostrophic model. *Tellus* **6** (6), 273–286.
- PLOUGONVEN, R., MURAKI, D. J. & SNYDER, C. 2005 A baroclinic instability that couples balanced motions and gravity waves. *J. Atmos. Sci.* **62**, 1545–1559.
- PLOUGONVEN, R. & SNYDER, C. 2005 Gravity waves excited by jets: propagation versus generation. *Geoph. Res. Lett.* **32** (L18802). doi:10.1029/2005GL023730.
- PLOUGONVEN, R. & SNYDER, C. 2007 Inertia–gravity waves spontaneously generated by jets and fronts. Part I. Different baroclinic life cycles. *J. Atmos. Sci.* **64**, 2502–2520.
- PLOUGONVEN, R., TEITELBAUM, H. & ZEITLIN, V. 2003 Inertia–gravity wave generation by the tropospheric mid-latitude jet as given by the fastex radiosoundings. *J. Geophys. Res.* **108** (D21), 4686.
- PLOUGONVEN, R. & ZEITLIN, V. 2002 Internal gravity wave emission from a pancake vortex: an example of wave-vortex interaction in strongly stratified flows. *Phys. of Fluids* **14** (3), 1259–1268.
- POULIN, F. J. & FLIERL, G. R. 2003 The nonlinear evolution of barotropically unstable jets. *J. Phys. Oceanogr.* **33**, 2173–2192.
- RIPA, P. 1983 General stability conditions for zonal flows in a one-layer model on the β -plane or the sphere. *J. Fluid Mech.* **126**, 463–489.
- SAKAI, S. 1989 Rossby–Kelvin instability: a new type of ageostrophic instability caused by a resonance between rossby waves and gravity waves. *J. Fluid Mech.* **202**, 149–176.
- SKAMAROCK, W. C., KLEMP, J. B., DUDHIA, J., GILL, D. O., BARKER, D. M., WANG, W. & POWERS, J. G. 2005 A description of the Advanced Research WRF Version 2. *Tech Note*. NCAR.
- STONE, P. H. 1966 On non-geostrophic baroclinic instability. *J. Atmos. Sci.* **23**, 390–400.
- STONE, P. H. 1970 On non-geostrophic baroclinic instability. Part 2. *J. Atmos. Sci.* **27**, 721–726.
- SUTYRIN, G. G. 2007 Ageostrophic instabilities in a horizontally uniform baroclinic flow along a slope. *J. Fluid Mech.* **588**, 463–473.
- TOKIOKA, T. 1970 Non-geostrophic and non-hydrostatic stability of a baroclinic fluid. *J. Meteorol. Soc. Jpn* **48**, 503–520.
- TREFETHEN, L. N. 2000 *Spectral Methods in MATLAB*. Society for Industrial and Applied Mathematics.

- VANNESTE, J. 1993 The Kelvin–Helmoltz instability in a non-geostrophic baroclinic unstable flow. *Math. Comput. Modelling* **17**, 149–154.
- VANNESTE, J. & YAVNEH, I. 2004 Exponentially small inertia–gravity waves and the breakdown of quasi-geostrophic balance. *J. Atmos. Sci.* **61**, 211–223.
- VANNESTE, J. & YAVNEH, I. 2007 Unbalanced instabilities of rapidly rotating stratified shear flows. *J. Fluid Mech.* **584**, 373–396.
- WICKER, L. J. & SKAMAROCK, W. C. 2002 Time splitting methods for elastic models using forward time schemes. *Mon. Weath. Rev.* **130**, 2088–2097.
- WILLIAMS, P. D., HAINE, T. W. N. & READ, P. L. 2005 On the generation mechanisms of short-scale unbalanced modes in rotating two-layer flows with vertical shear. *J. Fluid Mech.* **528**, 1–22.
- WUNSCH, C. & FERRARI, R. 2004 Vertical mixing energy and the general circulation of the oceans. *Annu. Rev. Fluid Mech.* **36**, 281–314.